Gallium Sulfide–Single-Walled Carbon Nanotube Composites: High-Performance Anodes for Lithium-Ion Batteries

*Xiangbo Meng, Kai He, Dong Su, Xiaofeng Zhang, Chengjun Sun, Yang Ren, Hsien-Hau Wang, Wei Weng, Lynn Trahey, Christian P. Canlas, and Jeffrey W. Elam**

Metal sulfides are an important class of functional materials possessing exceptional electrochemical performance and thus hold great promise for rechargeable secondary batteries. In this work, we deposited gallium sulfide (GaS_x, x = 1.2) thin films by atomic layer deposition (ALD) onto single-walled carbon nanotube (SWCNT) powders. The ALD GaS_x was performed at 150 °C, and produced uniform and conformal amorphous films. The resulting core-shell, nanostructured SWCNT-GaS_x composite exhibited excellent electrochemical performance as an anode material for lithium-ion batteries (LIBs), yielding a stable capacity of ≈575 mA g^{-1} at a current density of 120 mA g^{-1} in the voltage window of 0.01–2 V, and an exceptional columbic efficiency of >99.7%. The GaS_x component of the composite produced a specific capacity of 766 mA g^{-1}, a value two times that of conventional graphite anodes. We attribute the excellent electrochemical performance of the composite to four synergistic effects: 1) the uniform and conformal ALD GaS_x coating offers short electronic and Li-ion pathways during cycling; 2) the amorphous structure of the ALD GaS_x accommodates stress during lithiation-delithiation processes; 3) the mechanically robust SWCNT framework also accommodates stress from cycling; 4) the SWCNT matrix provides a continuous, high conductivity network.

1. Introduction

To address the vexing problems of depleting fossil fuel reserves and rising greenhouse gas levels, renewable energy sources such as solar radiation, wind, and waves[1] are undergoing intensive investigation. All of these renewable sources are intermittent, and will require energy storage technologies, such as batteries, to produce a continuous power flow. Electric vehicles (EVs) can also play a role in solving these challenges, but again, substantial improvements in battery performance are required to realize their full potential. Lithium-ion batteries (LIBs) are promising candidates for fulfilling the energy storage requirements of renewable power and EVs. LIBs, consisting of a $LiCoO_2$ cathode and a graphite anode, have dominated the consumer electronics market since their introduction in 1991,[2] primarily due to their superior energy and power density compared to other secondary batteries. However, to meet the demanding requirements for EVs, the specific energy of LIBs must increase by 2–5 times from the current value of 150 Wh kg^{-1}.[3] As a consequence, the quest for higher-performance electrode materials with increased power, energy density, lifetime, and safety is ongoing. In particular, nanomaterials are regarded as having great potential to enhance LIB performance as a result of their reduced dimensions.[4] Of the many classes of nanophase materials investigated to date, metal sulfides are relatively unexplored, but show great potential to serve as either electrodes [5] (e.g. MnS, FeS/FeS_2, CuS, and ZnS), or lithium-ion conducting solid electrolytes (e.g., $Li_{10}GeP_2S_{12}$)[6] and consequently they are a promising avenue of research.

Atomic layer deposition (ALD) is a technique for producing nanophase materials[7] that has recently achieved a series of successes in improving LIB performance.[8] ALD uses alternating exposures between two or more precursor vapors and a solid surface to deposit material in an atomic layer-by-layer fashion.[9] The unique aspect of ALD compared to conventional chemical and physical vapor deposition (CVD and PVD), is that the different precursors are supplied individually, and they react with the surface in a self-limiting manner.[9] As

Dr. X. Meng, Dr. C. P. Canlas, Dr. J. W. Elam
Energy Systems Division
Argonne National Laboratory
9700 South Cass Avenue
Argonne, IL 60439, USA
E-mail: jelam@anl.gov
Dr. X. Zhang, Dr. W. Weng, Dr. L. Trahey
Chemical Sciences and Engineering Division
Argonne National Laboratory
9700 South Cass Avenue
Argonne, IL 60439, USA
Dr. C. Sun, Dr. Y. Ren
Advanced Photon Source
Argonne National Laboratory
9700 South Cass Avenue
Argonne, IL 60439, USA
Dr. H.-H. Wang
Materials Science Division
Argonne National Laboratory
9700 South Cass Avenue
Argonne, IL 60439, USA
Dr. K. He, Dr. D. Su
Center for Functional Nanomaterials
Brookhaven National Laboratory
Upton, NY 11973, USA

DOI: 10.1002/adfm.201401002

a result, ALD films are exquisitely conformal and uniform, even on high surface area or high aspect ratio substrates, and the film thickness and composition can be controlled at the atomic level. A broad range of materials can be synthesized by ALD, and to date, these include over different metal sulfides reported, including ZnS,[10] CdS,[11] CaS,[12] BaS,[13] SrS,[13] Cu_2S,[14] In_2S_3,[15] WS_2,[16] TiS_2,[17] PbS,[18] SnS,[19] $ZnIn_xS_y$,[20] and Cu_2ZnSnS_4.[21]

Recently, we extended this list of ALD metal sulfides to include gallium sulfide (GaS_x, x ≈ 1.2), prepared using hexakis(dimethylamido)digallium ($Ga_2(NMe_2)_6$) and hydrogen sulfide (H_2S) in the temperature range 150–200 °C.[22] Based on our in situ measurements and ex situ characterization, we proposed the following mechanism for the GaS_x ALD:

$$\left|-(SH)_y + Ga(N(CH_3)_2)_3(g) \rightarrow \right| - S_y - Ga(N(CH_3)_2)_{(3-y)} + yHN(CH_3)_2(g) \quad (1)$$

$$\left|-S_y - Ga(N(CH_3)_2)_{(3-y)} + 1.5H_2S(g) \rightarrow \right| - (GaS_{1.5}) - (SH)_y + (3-y)HN(CH_3)_2(g) \quad (2)$$

in which the symbol "|–" represents the surface, "(g)" denotes gaseous phase, and the monomeric Ga compound is used for simplicity. In Equation (1a), the Ga compound reacts with y thiol groups (–$(SH)_y$ where y = 0–3) liberating y of the three dimethylamido- ligands (i.e., –$N(CH_3)_2$) into the gas phase. In Equation (1b), the H_2S removes the remaining (3–y) dimethylamido- ligands into the gas phase to form Ga_2S_3, and repopulate the surface with thiols. Our measurements revealed that y varied with deposition temperature from y = 1.8 at 125 °C to y = 0.1 at 225 °C. The gallium sulfide surface reactions Equation (1a)–(1a) were self-limiting over this temperature range, but the ALD growth per cycle varied from 1.0 Å $cycle^{-1}$ at 125 °C to 0.5 Å $cycle^{-1}$ at 225 °C. We found that the S/Ga ratio was 1.0–1.2 in the range of 125–200 °C, and that the films were amorphous. Both of these properties resulted from residual dimethylamido-ligands in the films. Significantly, our electrochemical testing showed the ALD GaS_x nanofilms to be a promising lithium-ion battery anode material for microbatteries, exhibiting reliable cyclability and a high specific capacity of 770 mAh g^{-1} at a current density of 320 mA g^{-1} in the voltage window of 0.01–2.00 V.[22]

In a previous study,[23] commercial micro-Ga_2S_3 powder was evaluated for use as an LIB electrode material, and it was claimed to yield a theoretical capacity of 1137 mAh/g. In spite of its distinctive discharge-charge behaviors, the micro-Ga_2S_3 suffered from severe capacity fading, accounting for a capacity drop from 1100 mAh g^{-1} at the 1st cycle to ≈400 mAh g^{-1} at the 20th cycle. Herein, we report that ALD produces nano-sized GaS_x with dramatically improved performance compared to the commercial micro-Ga_2S_3 powder. By depositing the ALD GaS_x on single-walled carbon nanotubes (SWCNTs), we synthesized a SWCNT-GaS_x nanophase composite. This composite showed exceptional specific capacity and long cyclability, and has great promise as a higher performance alternative compared to conventional graphite LIB anodes.

2. Results and Discussion

The uncoated SWCNTs were characterized by SEM and TEM (Figure SI-1 in Supporting Information), and found to be comprised of 5–10 nm bundles consisting of 10–100 predominantly single-walled CNTs. **Figure 1**a shows a TEM image of a pair of neighboring, 1.4 nm SWCNTs, and also a bundle of SWCNTs with an outer diameter of 9 nm. In addition to forming bundles, the SWCNTs have a high concentration of physical defects along their side walls. Figures 1b–d show TEM images of a small quantity (≈5 mg) of the SWCNT sample following 50, 100, and 150 ALD GaS_x cycles, respectively, using the timing sequence 5–5–5–5 s. It is evident that the SWCNTs were uniformly and conformally coated with the ALD GaS_x film to thicknesses of 2.5, 6.4, and 11.1 nm, respectively. It should be noted that pure, individual SWCNTs are generally inert towards ALD chemistry, so that the growth per cycle (GPC) remains near zero for many hundreds of cycles.[24–26] In contrast, our SWCNT material yielded relatively high GPC values of 0.5, 0.78, and 0.94 Å $cycle^{-1}$ after the 50, 100, and 150 GaS_x ALD cycles, respectively. The expected value for GaS_x ALD is 1.0 Å $cycle^{-1}$ at this temperature, indicating that the GaS_x growth is still somewhat inhibited on the SWCNT substrate for the initial 100–150 cycles. The 150 cycle sample was further characterized by STEM imaging (Figure 1e) and by EELS elemental mapping (Figure 1f–i). Figure 1e reveals that the SWCNT network is uniformly encapsulated by the ALD GaS_x film to form a nanoscale composite material. The EELS maps in Figures 1g–i correspond to the boxed region in Figure 1f, and clearly demonstrate that the coating is uniform and comprised of Ga and S.

Next, we proceeded to coat 100 mg SWCNT batches with 150 cycles ALD GaS_x using the timing sequence 120–120–120–120 s, and found that the weight of the SWCNTs increased from 100 mg to 335 mg, implying a composition of 70 wt% GaS_x. This sample was then characterized using FESEM (**Figure 2** and Figure SI-2). Figures 2a and 2b show the same region of the SWCNT sample before and after the ALD GaS_x and confirm that the ALD coating increases the diameter of all of the SWCNTs uniformly, and converts the material from a porous, open powder into a densified composite. EDX mapping (Figures 2c–e) of the coated specimen shown in the SEM image of Figure 2c, are consistent with a uniform GaS_x coating on the SWCNTs, consistent with our observation of the 5 mg sample. In summary, the GaS_x ALD converts the SWCNTs into a core-shell, SWCNT-GaS_x nanocomposite. Moreover, we can fabricate these materials in sufficient quantities for electrochemical evaluation.

We further characterized the bare SWCNT and the SWCNT-GaS_x composite materials, as well as the commercial Ga_2S_3, using XRD and Raman measurements. As expected, XRD (**Figure 3**a) showed the commercial Ga_2S_3 to be a crystalline α-Ga_2S_3 (PDF # 30–0577). In contrast, both the SWCNTs and the SWCNT-GaS_x composite appear relatively featureless by XRD, with the exception of a broad, weak peak at 26.8° for the two, consistent with the (002) plane of graphite (PDF # 41–1487). There also appears to be a broad, weak peak at 19° for the SWCNT-GaS_x composite sample that corresponds to the (–202) feature for α-Ga_2S_3. Raman measurements of the SWCNTs and the SWCNT-GaS_x composite (Figures 3b,c)

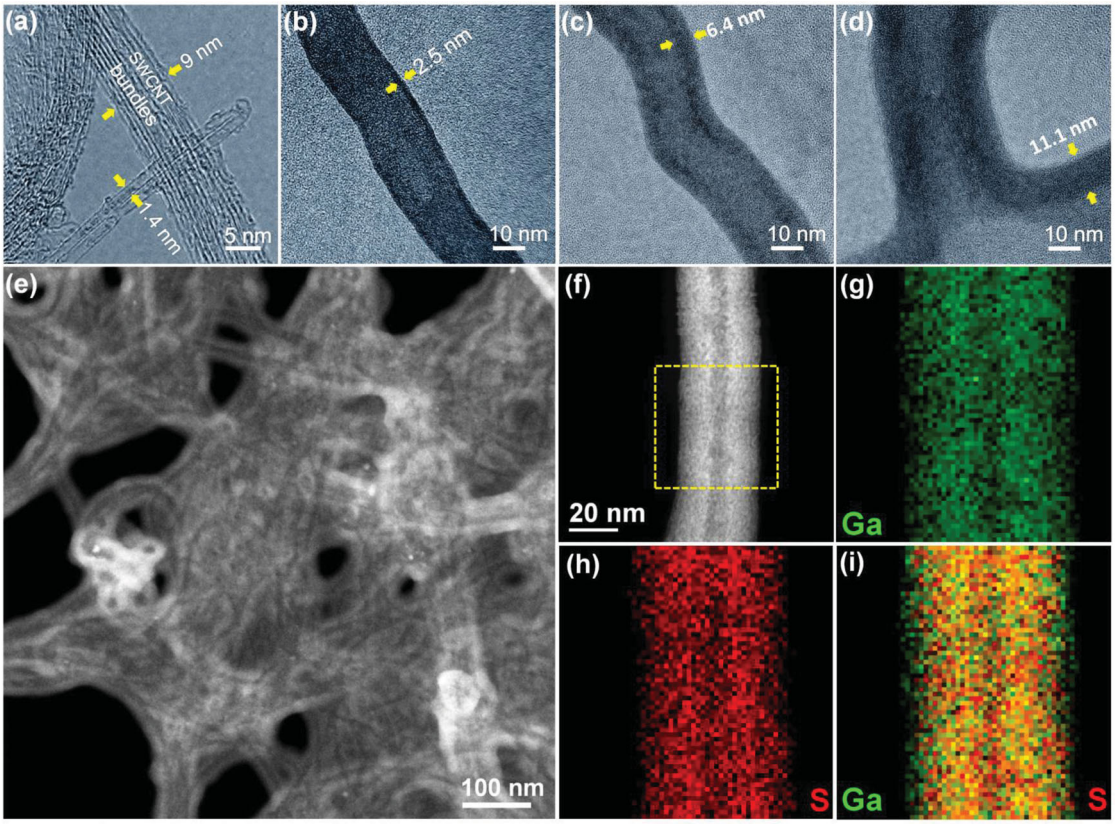

Figure 1. TEM a–d) and STEM e–i) images of: a) SWCNTs and their bundles; SWCNTs coated by b) 50-cycle, c) 100-cycle, and d) 150-cycle ALD GaS_x; e,f) ADF-STEM images; and STEM-EELS mapping of g) gallium, h) sulfur, and i) both gallium and sulfur.

exhibited more structure, as expected based on the greater sensitivity of Raman to short-range order. The black traces in Figures 3(b) and (c) exhibit the characteristic features of SWCNTs: the radial breathing mode (RBM) at 218, 254, and 280 cm^{-1}, D band at 1303 cm^{-1}, G band at 1552 and 1591 cm^{-1}, M band at 1720 and 1920 cm^{-1}, and G band at 2607 cm^{-1}.[27–29] The RBM at 218 cm^{-1} indicates the presence of bundles,[29] while the RBM features at 254 and 280 cm^{-1} reveal the semiconducting nature of SWCNTs.[29] This property is also supported by the characteristic splitting of the G band.[27] Furthermore, the presence of the D band implies an abundance of defects,[27–29] consistent with the facile nucleation of the GaS_x ALD, which relies on defect sites on the SWCNT surface. For isolated SWCNTs, the correlation [27,30] between nanotube diameter (d_t) and breathing mode frequency (ω_{RBM}) is $d_t = 248\ cm^{-1}\ nm/\omega_{RBM}\ cm^{-1}$. The appearance of RBM features at 254 and 280 cm^{-1} implies nanotube diameters of 1.0 and 0.9 nm, in fair agreement with the TEM measurements (Figure 1a). Raman spectra of the commercial Ga_2S_3 (blue traces in Figures 3(b) and (c)) are consistent with crystalline Ga_2S_3.[31] The dominant peaks at 233 and 386 cm^{-1} are due to the ν_4 and ν_1 modes of the GaS_4 molecular unit, respectively. In addition, the features at 114, 140, 147, 307, 329, 340, 350, and 422 cm^{-1} are also characteristic of crystalline Ga_2S_3.[31–33] Raman spectra of the SWCNT-GaS_x composite (Red traces in Figures 3b,c) show all of the peaks present in the SWCNT spectrum, and new peaks appearing at ≈150, 165, 175, 220, 310, and 385 cm^{-1}. The peaks at 150, 310, and 385 cm^{-1} are also present in the Ga_2S_3 spectrum, and the peak at 220 cm^{-1} might be a red-shifted version of the very intense 233 cm^{-1} feature for Ga_2S_3. This red-shift might result from a substitution of S in the GaS_4 units with heavier dimethylamido- ligands ($-N(CH_3)_2$) that exist as impurities in the ALD GaS_x films.[22] We also observed peaks at 2878 and 2941 cm^{-1} for the composite that appeared in the Ga_2S_3 spectrum, but are not previously reported. In conclusion, the Raman spectrum for the SWCNT-GaS_x composite is clearly different from the uncoated SWCNT, and has some of the features expected for Ga_2S_3.

Following synthesis and characterization, the SWCNT-GaS_x composite was electrochemically tested, along with the SWCNT and Ga_2S_3 standards, to evaluate their performance as LIB anode materials. The charge-discharge profiles versus potential for these three materials are shown in **Figures 4**a,c,e, while the corresponding dQ/dV curves are given in Figures 4b,d,f for the commercial Ga_2S_3, SWCNTs, and SWCNT-GaS_x, respectively. During the first five charge-discharge cycles for the commercial Ga_2S_3 (Figure 4a), there is a large plateau at ≈1.0 V with the 1st discharge (reduction, or lithiation) profile, mainly attributed to lithiation of the Ga_2S_3 electrode.[23] In addition, there is another declining plateau at ≈0.2 V in the 1st discharge. In the subsequent 1st charge (oxidation, or delithiation), three increasing plateaus are seen at ≈0.2, 0.8, and 1.6 V. The total 1st discharge capacity is 1334 mAh g^{-1}, higher than the theoretical capacity of 1137 mAh g^{-1}. We attribute this discrepancy

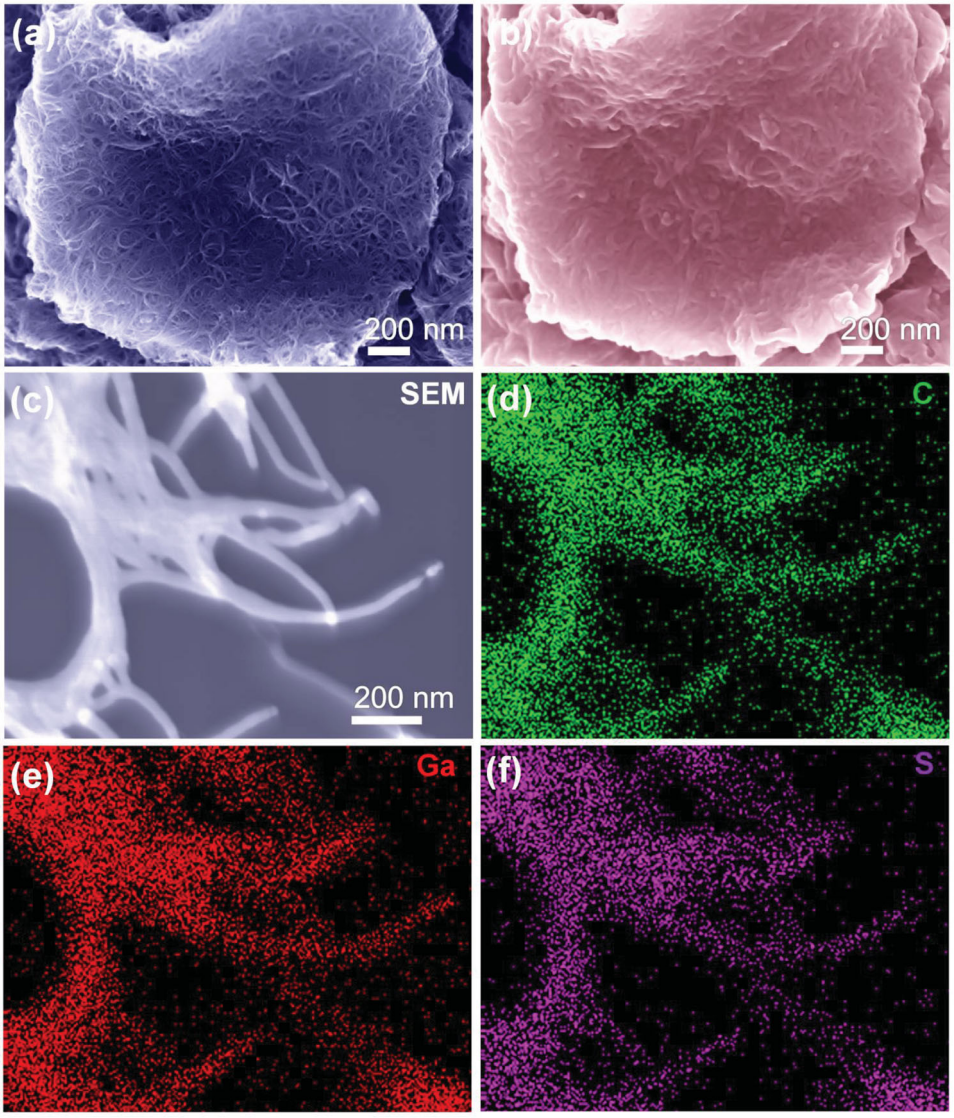

Figure 2. a–c) SEM and d–f) EDX mapping images of: a) SWCNTs and b,c) 150-cycle ALD GaS_x coated SWCNTs, and EDX mapping of: d) carbon, e) gallium, and f) sulfur on 150-cycle ALD GaS_x coated SWCNTs.

to the formation of a solid electrolyte interphase (SEI), which consumes extra current and lithium ions. In the subsequent 1st charge, the capacity reaches 880 mAh/g with the gradually increasing potential to 2.0 V. Apparently, there is an irreversible capacity of >450 mAh g^{-1} after the 1st cycle. Beginning with the 2nd discharge, the plateau at ≈1.0 V disappeared but two new plateaus appeared at ≈1.2 and ≈0.8 V. In addition, the plateau at 0.2 persisted. In contrast, the 2nd and following charge profiles showed similar behaviors to the 1st one, but their plateaus evolved with increasing cycles.

The discharge and charge capacities for the commercial Ga_2S_3 continuously decreased in the first five cycles. These charge-discharge characteristics are confirmed in the corresponding dQ/dV curves, Figure 4b. However, the dQ/dV curves further disclose that the reduction and oxidation peaks continued to evolve with extended testing up to 50 cycles. An evident phenomenon is that all of the reduction and oxidation peaks reduce in intensity. In particular, the peaks at >1.0 V almost disappear after the first 20 cycles, implying a continuous decline in redox and therefore significant irreversible capacity fading. Obviously, the commercial Ga_2S_3 cannot sustain stable electrochemical cycling, and is unsuitable as a LIB anode material.

SWCNTs have been widely investigated as LIB anodes in previous studies. They possess a high theoretical surface area of 2630 m^2 g^{-1} as a result of their small size and hollow core.[34] In Figure 4(c), the 1st discharge profile of the SWCNTs exhibits a declining plateau at ≈0.8 V and reaches a capacity of 1586 mAh g^{-1}. The subsequent 1st charge profile shows an increasing plateau at 1.2 V and reaches a total capacity of 222 mAh g^{-1}. The irreversible capacity of >1300 mAh g^{-1} is commonly attributed to the formation of the SEI on the SWCNTs, and the large value reflects the very high surface area.[35,36] Beginning with the 2nd charge-discharge cycle, the

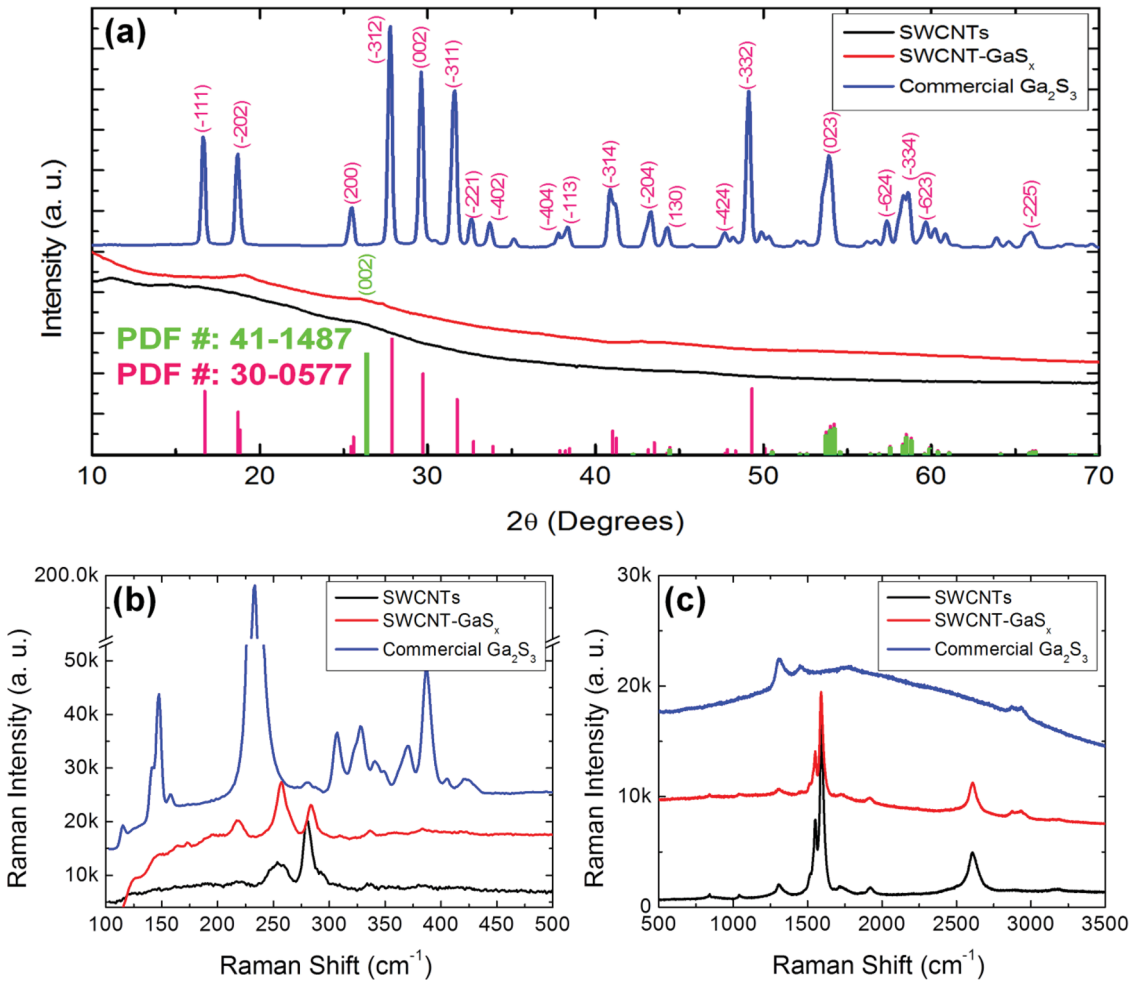

Figure 3. XRD measurements (a) and Raman spectra (b, c) of SWCNTs, Ga_2S_3, and SWCNT-GaS_x composite.

capacity fading becomes progressively smaller over the first five cycles. The corresponding dQ/dV profiles (Figure 4d) clearly show a reduction peak at 0.8 V in the first discharge that disappears in the following discharges, consistent with the extensive SEI formation in the 1st discharge. Another reduction peak appears at ≈0.02 V, which gradually decreases and stabilizes after several tens of cycles. In the 1st oxidation, peaks are seen at 0.3, 1.2, and 2.0 V. With increasing cycles, only the 0.02 V reduction peak remains while the oxidation peaks stabilize at 0.1 and 1.98 V. Apparently, the charge-discharge performance of the SWCNTs stabilizes with cycling, but this material provides only a limited capacity of <200 mAh g^{-1}, as previously observed.[37]

The charge-discharge profiles for the first 5 cycles of the SWCNT-GaS_x composite are shown in Figure 4e, and exhibit some of characteristics of both the Ga_2S_3 and the SWCNTs components. In the 1st discharge, the composite reaches a capacity of 2118 mAh g^{-1}, and shows a declining plateau at ≈0.88 V. The subsequent 1st charge shows three increasing plateaus at ≈0.2, 0.8, and 1.6 V, achieving a capacity of 810 mAh/g. Thus, the irreversible capacity is ≈1300 mAh g^{-1}, most probably from SEI formation on the high surface area of the composite. In the following cycles, the capacities gradually decreased but much more slowly compared to the commercial Ga_2S_3. The dQ/dV profiles (Figure 4f) clearly show two reduction peaks at 0.88 and 0.02 V, and four oxidation peaks at 0.36, 0.89, 1.2, and 1.6 V in the first reduction and oxidation, respectively. The peaks stabilize at 0.66 and 0.02 V for reduction, and at 0.2, 0.45, 0.8, and 0.86 V for oxidation. In comparison, the SWCNT-GaS_x composite demonstrated much better performance than the commercial Ga_2S_3 and the SWCNTs.

To directly compare the performance of the three materials, their cyclability and columbic efficiency data are plotted together in **Figure 5**. Using a current density of 120 mAh g^{-1}, both the SWCNTs and the SWCNT-GaS_x exhibit exceptional cyclability over 100 cycles (Figure 5a). Although both show a rapid capacity decrease during the initial 10 cycles, this behavior diminishes so that after ≈30 cycles the capacity becomes nearly constant. As a consequence, the SWCNTs maintain a discharge capacity of 130 mAh g^{-1} while the SWCNT-GaS_x composite sustains a capacity of 575 mAh g^{-1} at the 100th cycle. By contrast, the capacity of the commercial Ga_2S_3 drops continuously so be only 230 mAh g^{-1} at the 50th cycle.

The SWCNT-GaS_x composite demonstrated the best combination of specific capacity and capacity retention in Figure 5a. In addition, the SWCNT-GaS_x shows the highest

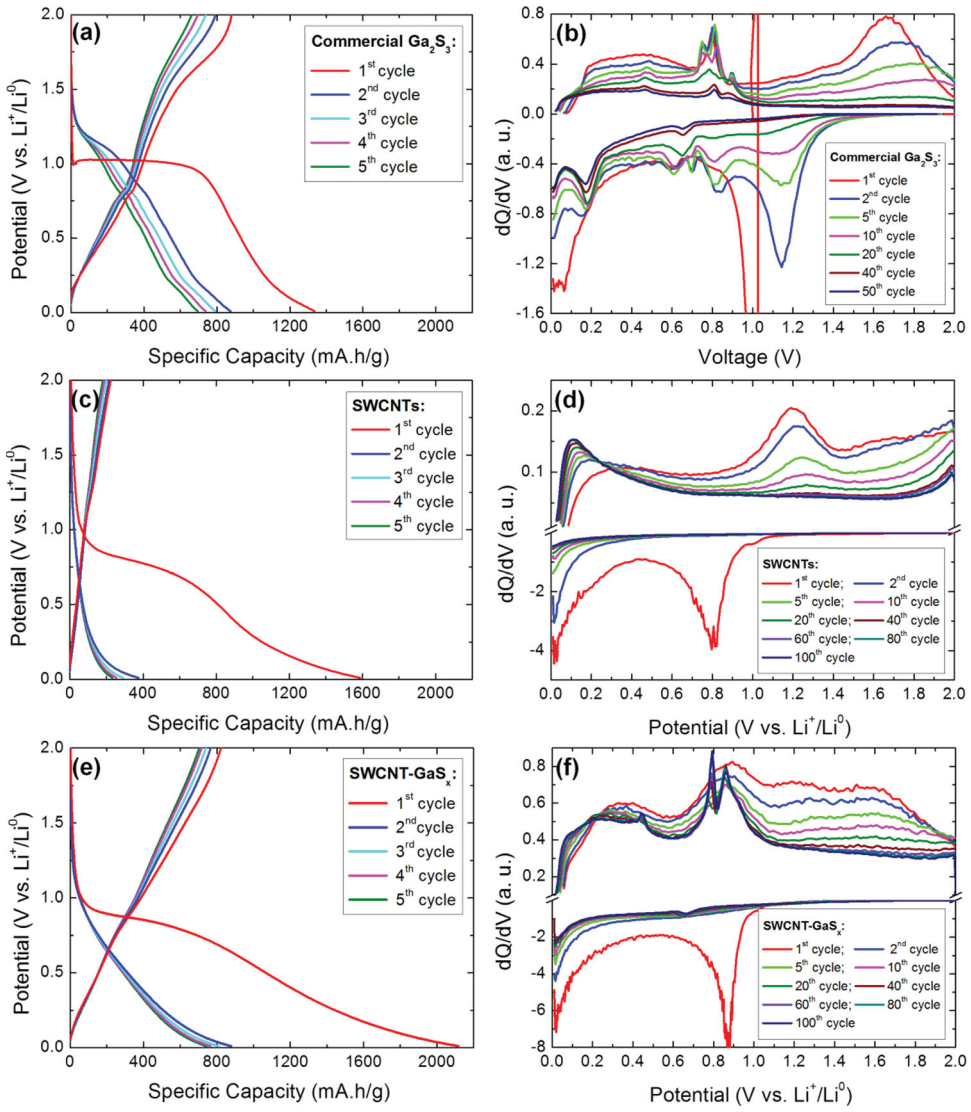

Figure 4. a,c,e) Discharge-charge profiles and b,d,f) the dQ/dV curves for a,b) commercial Ga_2S_3, c,d) commercial SWCNTs, and e,f) SWCNT-GaS_x composite.

columbic efficiency of the three materials, amounting to 99.7% at the 100th cycle compared to 98% for both the SWCNTs at the 100th cycle and the commercial Ga_2S_3 at the 50th cycle (Figure 5a). From the SWCNT-GaS_x composite data in Figure 5a and the known composition of the composite, we determined the capacity arising solely from the GaS_x, and this data is presented in Figure 5b. The ALD GaS_x exhibited very reliable cyclability and a capacity of 766 mAh g^{-1} at the 100th cycle, a value two times higher than graphite (372 mAh g^{-1}). In addition, the columbic efficiency reached 99.8% at the 100th cycle.

To explore the rate capability of the SWCNT-GaS_x composite, a higher current density of 600 mA g^{-1} was used (five times that of Figure 5). In contrast to the continuous capacity fading for the commercial Ga_2S_3 at this higher current (**Figure 6**), the SWCNT-GaS_x demonstrates a much slower capacity fading in the first 30 cycles, and then gradually stabilizes at a sustained value of 514 mAh g^{-1} at the 100th cycle. Once again, the SWCNT-GaS_x composite shows much better columbic efficiency compared to the commercial Ga_2S_3, amounting to 99.7% for the composite and ≈98% for the commercial Ga_2S_3. In conclusion, the SWCNT-GaS_x composite has a very good rate capability.

The excellent performance of the SWCNT-GaS_x composite can be attributed to synergic effects that arise from combining the SWCNTs and GaS_x constituents at the nano-scale. In the first place, GaS_x is an insulator with a relatively high Li storage capacity, while the SWCNTs have a very high conductivity but only a modest Li storage capacity. Consequently, combining the two materials provides the optimal combination of high electrical conductivity and capacity. Second, the very thin (≈10 nm) GaS_x coating ensures rapid electrical and Li-ionic transport, both of which benefit the capacity and rate properties. Third, the amorphous structure of the ALD GaS_x can minimize the loss of structural integrity from volume changes that generally accompanies conversion reactions in metal sulfides. Fourth, the continuous SWCNT network can provide both high electrical

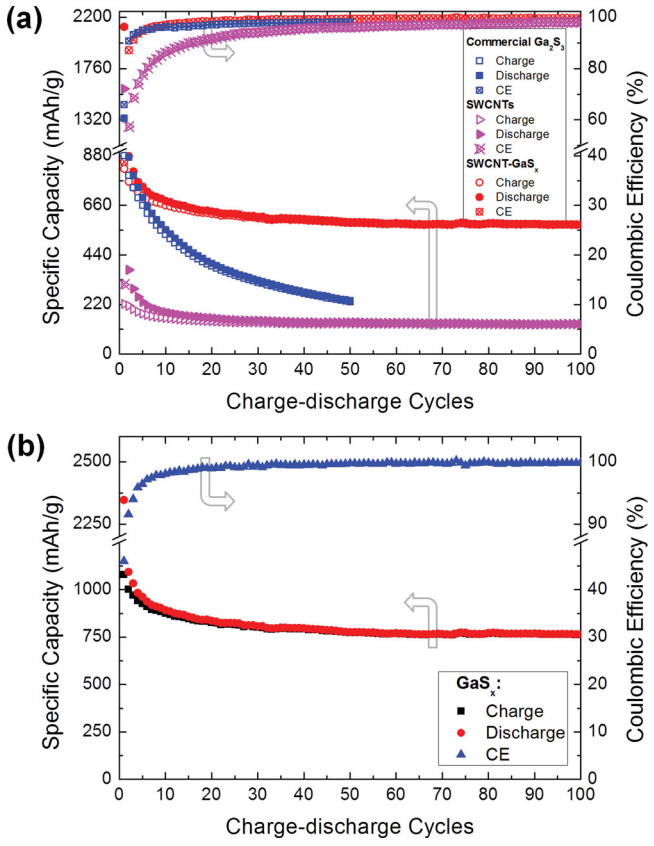

Figure 5. a) Cycling performance and columbic efficiency for commercial Ga_2S_3, commercial SWCNTs, and SWCNT-GaS_x composite at 120 mA g^{-1}. b) Cycling performance and columbic efficiency for the GaS_x component of the SWCNT-GaS_x composite at 120 mA g^{-1}.

conductivity, and structural reinforcement to the composite to minimize stress-induced deterioration during cycling. In contrast, the commercial Ga_2S_3 is crystalline and micro-sized, and lacks the conductive support to accommodate stress and improve electrical transport. On the other hand, the SWCNTs suffer from a relatively low capacity, similar to graphite.

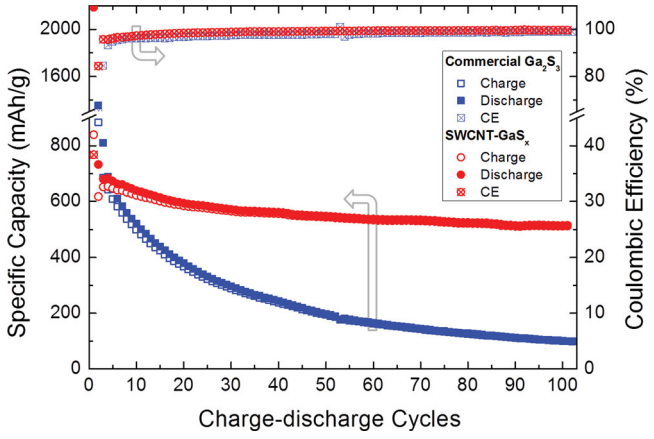

Figure 6. Cycling performance and columbic efficiency of commercial Ga_2S_3 and SWCNT-GaS_x composite at 600 mA/g.

3. Conclusions

The ALD of GaS_x thin films on a SWCNT support yields a nanocomposite material comprised of a conductive carbon core encapsulated by a uniform and conformal, amorphous, GaS_x shell. This material demonstrated exceptional electrochemical performance in charge-discharge testing of LIBs, with a high specific capacity, stable cycling behavior, and excellent columbic efficiency. The enhanced performance compared to SWCNT and commercial Ga_2S_3 is believed to derive from synergistic effects between the SWCNT and GaS_x components. Our results indicate that the SWCNT-GaS_x composite is a promising, high-performance anode material that could replace conventional graphite anodes. In the future, the SWCNT-GaS_x composites might be optimized to serve this role by: 1) Adjusting the GaS_x fraction to achieve the best balance of capacity and conductivity; 2) Utilizing graphitic frameworks with tailored pore sizes to facilitate transport from the electrolyte; and 3) Optimizing the porosity and void space to best accommodate stress induced by volume changes.

4. Experimental Section

The GaS_x ALD was conducted at 150 °C in a custom, viscous flow ALD reactor,[38] comprised of a heated stainless steel tube with an inner diameter of 5 cm and a length of 100 cm. Prior to the GaS_x ALD, SWCNTs (Sigma-Aldrich, USA) powder was loaded into a porous container and placed in the reactor. The reactor was then purged using ultrahigh purity (UHP, 99.999%) nitrogen carrier gas at 300 sccm at a pressure of ~1.0 Torr. The GaS_x ALD was performed using alternating exposures to $Ga_2(NMe_2)_6$ (98%, Strem Chemical, Inc., USA) and 1% H_2S (balanced by N_2, Matheson Tri-gas, USA) with a purging period of pure N_2 flow between each exposure. The ALD timing sequence is designated as: t_1–t_2–t_3–t_4, corresponding to the durations of the $Ga_2(NMe_2)_6$ exposure, first N_2 purge, H_2S exposure, and second N_2 purge, respectively, with all times in seconds (s). Two different timing sequences were used in this study: 5–5–5–5 s for coating small quantities (≤5 mg) of SWCNTs, and 120–120–120–120 s for coating larger, 100 mg quantities of SWCNTs. To boost the $Ga_2(NMe_2)_6$ vapor pressure, the solid compound was heated to 100 °C in a temperature-controlled, stainless steel bubbler. The SWCNT samples were typically coated using 50–150 ALD GaS_x cycles to produce films with a thickness of ≈2.5 to 11.1 nm.

The SWCNT-GaS_x composites were characterized by using a field emission scanning electron microscope (FE-SEM, Hitachi S4700) equipped with energy dispersive X-ray spectroscopy (EDX) for elemental analysis. Transmission electron microscopy (TEM, JEOL 2100F) was utilized to evaluate the microstructure of the pristine SWCNTs, and to determine the GaS_x coating thickness. In addition, aberration-corrected scanning transmission electron microscopy (STEM, Hitachi HD2700C) was used to perform high-angle annular dark-field (HAADF) imaging and energy-loss spectroscopy (EELS) elemental mapping of the coated samples.

Synchrotron-based X-ray diffraction (XRD) was used to characterize the crystallinity of the SWCNT-GaS_x composites as well as commercial microsized Ga_2S_3 powder (Sigma-Aldrich), and the pristine SWCNTs. The XRD measurements were conducted at beamline 11-ID-C of the Advanced Photon Source (APS), Argonne National Laboratory (ANL, IL, USA), using an X-ray wavelength of 0.108 Å. Room temperature Raman spectra (Renishaw) were recorded at a resolution of 1 cm^{-1} in back scattering (180°) configuration using 632.8 nm excitation.

The SWCNT-GaS_x composite powder was mixed with Super P carbon black and polyvinylidene fluoride (PVDF, Sigma-Aldrich) using a ratio of 8:1:1 and dissolved in a N-methyl-2-pyrrolidone (NMP, Sigma-Aldrich)

solvent for fully homogenous mixing. The resultant slurry was cast onto a Cu foil and expanded into a laminate using a 50 μm doctor blade. The laminate was then dried in a furnace at 80 °C within an Ar-filled glove box for 24 hours. Next, the dried laminate was punched into 9/16 inch circular electrodes and subsequently assembled into CR2032 LIB coin cells in an Ar-filled glove box with H_2O and O_2 levels below 1 ppm. Li metal was used as the counter/reference electrode, a Celgard 2325 membrane was used as the separator, and 1 M lithium bis(trifluoromethanesulfonyl) imide (LITFSI, Sigma Aldrich) in 1,3-dioxolane (DOL, Sigma Aldrich) and 1,2-dimethoxyethane (DME, Sigma Aldrich) (DOL:DME = 1:1 by volume) was used as the electrolyte. The discharge-charge testing was performed on a MACCOR 4200 battery tester using a voltage window of 0.01–2.0 V for the SWCNT-GaS_x electrodes. In addition, control samples were assembled and tested following the same procedures described above using laminates prepared from the commercial SWCNTs and microsized Ga_2S_3 powder. All of the electrochemical testing was performed at room temperature.

Supporting Information

Supporting Information is available from the Wiley Online Library or from the author.

Acknowledgements

This work was supported as part of the Center for Electrical Energy Storage: Tailored Interfaces, an Energy Frontier Research Center funded by the US Department of Energy, Office of Science, Office of Basic Energy Sciences. Electron microscopy was performed at the Electron Microscopy Center for Materials Research (EMCMR) at Argonne National Laboratory. Use of the EMCMR was supported by the US Department of Energy, Office of Science, Office of Basic Energy Sciences, under Contract No. DE-AC02–06CH11357 operated by UChicago Argonne, LLC. The research carried out at the Center for Functional Nanomaterials, Brookhaven National Laboratory, was supported by the U.S. Department of Energy, Office of Basic Energy Sciences, under Contract No. DE-AC02–98CH10886. X. Meng appreciates the funding support of a NSERC Postdoctoral Fellowship, Canada.

Received: March 28, 2014
Published online: July 8, 2014

[1] J. B. Goodenough, Y. Kim, *Chem. Mater.* **2010**, *22*, 587.
[2] J. M. Tarascon, M. Armand, *Nature* **2001**, *414*, 359.
[3] M. M. Thackeray, C. Wolverton, E. D. Isaacs, *Energy Environ. Sci.* **2012**, *5*, 7854.
[4] P. G. Bruce, B. Scrosati, J. M. Tarascon, *Angew. Chem. Int. Ed.* **2008**, *47*, 2930.
[5] J. Cabana, L. Monconduit, D. Larcher, M. R. Palacin, *Adv. Mater.* **2010**, *22*, E170.
[6] N. Kamaya, K. Homma, Y. Yamakawa, M. Hirayama, R. Kanno, M. Yonemura, T. Kamiyama, Y. Kato, S. Hama, K. Kawamoto, A. Mitsui, *Nat. Mater.* **2011**, *10*, 682.
[7] J. Elam, in *Atomic Layer Deposition of Nanostructured Materials* (Eds.: N. Pinna, M. Knez), Wiley-VCH, Weinheim, **2012**, pp. 227.
[8] X. B. Meng, X. Q. Yang, X. L. Sun, *Adv. Mater.* **2012**, *24*, 3589.
[9] S. M. George, *Chem. Rev.* **2010**, *110*, 111.
[10] S. Farhangfar, R. B. Yang, M. Pelletier, K. Nielsch, *Nanotechnology* **2009**, *20*.
[11] J. T. Tanskanen, J. R. Bakke, S. F. Bent, T. A. Pakkanen, *J. Phys. Chem. C* **2010**, *114*, 16618.
[12] S. Dey, S. J. Yun, *Appl. Surf. Sci.* **1999**, *143*, 191.
[13] J. Ihanus, T. Hanninen, T. Hatanpaa, T. Aaltonen, I. Mutikainen, T. Sajavaara, J. Keinonen, M. Ritala, M. Leskela, *Chem. Mater.* **2002**, *14*, 1937.
[14] A. B. F. Martinson, J. W. Elam, M. J. Pellin, *Appl. Phys. Lett.* **2009**, *94*.
[15] S. K. Sarkar, J. Y. Kim, D. N. Goldstein, N. R. Neale, K. Zhu, C. M. Elliot, A. J. Frank, S. M. George, *J. Phys. Chem. C* **2010**, *114*, 8032.
[16] T. W. Scharf, S. V. Prasad, T. M. Mayer, R. S. Goeke, M. T. Dugger, *J. Mater. Res.* **2004**, *19*, 3443.
[17] V. Pore, M. Ritala, M. Leskela, *Chem. Vapor Depos.* **2007**, *13*, 163.
[18] N. P. Dasgupta, W. Lee, F. B. Prinz, *Chem. Mater.* **2009**, *21*, 3973.
[19] P. Sinsermsuksakul, J. Heo, W. Noh, A. S. Hock, R. G. Gordon, *Adv. Energy Mater.* **2011**, *1*, 1116.
[20] P. Genevee, F. Donsanti, G. Renou, D. Lincot, *J. Phys. Chem. C* **2011**, *115*, 17197.
[21] E. Thimsen, S. C. Riha, S. V. Baryshev, A. B. F. Martinson, J. W. Elam, M. J. Pellin, *Chem. Mater.* **2012**, *24*, 3188.
[22] X. Meng, J. A. Libera, T. T. Fister, H. Zhou, J. K. Hedlund, P. Fenter, J. W. Elam, *Chem. Mater.* **2014**, *26*, 1029.
[23] H. Senoh, H. Kageyama, T. Takeuchi, K. Nakanishi, T. Ohta, H. Sakaebe, M. Yao, T. Sakai, K. Yasuda, *J. Power Sources* **2011**, *196*, 5631.
[24] D. B. Farmer, R. G. Gordon, *Nano Lett.* **2006**, *6*, 699.
[25] A. S. Cavanagh, C. A. Wilson, A. W. Weimer, S. M. George, *Nanotechnology* **2009**, *20*.
[26] G. D. Zhan, X. H. Du, D. M. King, L. F. Hakim, X. H. Liang, J. A. McCormick, A. W. Weimer, *J. Am. Ceramic Soc.* **2008**, *91*, 831.
[27] M. S. Dresselhaus, G. Dresselhaus, A. Jorio, A. G. Souza, R. Saito, *Carbon* **2002**, *40*, 2043.
[28] S. S. Islam, K. A. Shah, H. S. Mavi, A. K. Shaukla, S. Rath, Harsh, *Bull. Mater. Sci.* **2007**, *30*, 295.
[29] F. Hennrich, R. Krupke, S. Lebedkin, K. Arnold, R. Fischer, D. E. Resasco, M. Kappes, *J. Phys. Chem. B* **2005**, *109*, 10567.
[30] A. Jorio, M. A. Pimenta, A. G. Souza, R. Saito, G. Dresselhaus, M. S. Dresselhaus, *N. J. Phys.* **2003**, *5*.
[31] H. T. Guo, H. Z. Tao, Y. B. Zhai, S. Mao, X. J. Zhao, *Spectrochim. Acta A- Mol. Biomol. Spectrosc.* **2007**, *67*, 1351.
[32] C. Julien, S. Barnier, I. Ivanov, M. Guittard, M. P. Pardo, A. Chilouet, *Mater. Sci. Eng. B-Solid State Mater. Adv. Technol.* **1999**, *57*, 102.
[33] J. Heo, J. M. Yoon, S. Y. Ryou, *J. Non-Cryst. Solids* **1998**, *238*, 115.
[34] Y. P. Wu, E. Rahm, R. Holze, *J. Power Sources* **2003**, *114*, 228.
[35] D. T. Welna, L. T. Qu, B. E. Taylor, L. M. Dai, M. F. Durstock, *J. Power Sources* **2011**, *196*, 1455.
[36] J. Eom, H. Kwon, *J. Mater. Res.* **2008**, *23*, 2458.
[37] S. H. Ng, J. Wang, Z. P. Guo, G. X. Wang, H. K. Liu, *Electrochim. Acta* **2005**, *51*, 23.
[38] J. W. Elam, M. D. Groner, S. M. George, *Rev. Sci. Instr.* **2002**, *73*, 2981.